A New Image Analysis Approach For Automatic Classification of Autistic Brains

Ayman El-Baz, et al.

IEEE, 2007

NeuroSpectrum Insights, Inc.
info@neurospectruminsights.com
www.neurospectruminsights.com

A NEW IMAGE ANALYSIS APPROACH FOR AUTOMATIC CLASSIFICATION OF AUTISTIC BRAINS

Ayman El-Baz[1], *Manuel F. Casanova*[2], *Georgy Gimel'farb*[3], *Meghan Mott*[2], *and Andrew E. Switwala*[2]

[1]Bioengineering Dept., University of Louisville, Louisville, KY, USA.
[2]Department of Psychiatry and Behavioral Science, University of Louisville, USA.
[3]Computer Science Department, University of Auckland, Auckland, New Zealand.

ABSTRACT

Autism is a developmental disorder characterized by social deficits, impaired communication, and restricted and repetitive patterns of behavior. Recent neuropathological studies of autism have revealed abnormal anatomy of the cerebral white matter (CWM) in autistic brains. In this paper we introduced a novel approach to classify autistic from normal subjects based on a new shape analysis of cerebral white matter gyrifications for both normal and autistic subjects. The proposed shape analysis technique consists of three main steps. The first step is to segment cerebral white matter from proton density MRI images using a priorly learned visual appearance model for the 3D cerebral white matter in order to control the evolution of deformable boundaries. The appearance prior is modeled with a translation and rotation invariant Markov-Gibbs random field of voxel intensities with a pairwise interaction model. The second step is to extract the gyrifications of cerebral white matter from the segmented cerebral white matter. The last step is to perform shape analysis to quantify the thickness of the extracted cerebral white matter gyrifications for both autistic and normal subjects. The preliminary results of the proposed image analysis has yielded promising results that would, in the near future, supplement the use of current technologies for diagnosing autism.

1. INTRODUCTION

Autism is an idiopathic developmental psychiatric disorder characterized by marked deficits in communication, social interaction, and interests. These deficiencies typically manifest themselves in stereotypic behavioral patterns that are restricted, repetitive, and ritualistic. During postnatal development, a significant percentage of autistic children exhibit macrocephaly and a concomitant increase in brain weight and volume (macroencephaly) [1]. The prevalence of children diagnosed with autism has rapidly increased during the last few decades. Although the reason for this rise in prevalence is debated in the literature, best estimates indicate that autism affects as many as 1 in 300 children [2]. The etiology of autism remains unclear, but research suggests a multifactorial diathesis (i.e., the interplay of genetic, developmental, and environmental factors) [3]. There is no cure for autism; however, therapies targeting specific symptoms may result in substantial improvement, particularly when started at a young age.

Neuroimaging and neuropathological studies have revealed a great deal concerning the pathogenesis of autism. An increase in cell packing and a reduction in cell size have been found in the limbic system of autistic individuals [4]. MRI studies have reported reductions in the corpus callosum in autistic subjects, but findings have been inconsistent as to which segment is abnormal [5, 6].

Recent neuropathological studies of autism have revealed abnormal anatomy of cerebral white matter (CWM) in autistic brains [7]. In addition, the deficits in the size of the corpus callosum and its sub-regions are well established in patients with autism relative to controls. In this work, we aim at using the reported abnormalities of CWM in order to devise robust classification methods of autistic vs. normal subjects through analysis of their respective MRIs. To overcome the limitations and shortcomings of the volumetric studies, our analysis is based on a new shape analysis in order to get accurate description of cerebral white matter gyrifications for both normal and autistic subjects.

2. METHODS

The objective of the proposed image analysis approach is to quantify the difference between the shape of cerebral white matter gyrifications for autistic subjects and controls (normals) without using traditional volumetric measurements. To achieve this goal an image analysis system consisting of three steps is proposed. These steps are: 1) segmentation of cerebral white matter from Proton Density MRI (PD-MRI) images, 2) extraction of cerebral white matter gyrifications from the segmented cerebral white matter, and 3) quantification of the thickness of cerebral white matter gyrifications.

All the proposed approaches in this paper have been run on the postmortem brains which were obtained from the Autism Tissue Program (ATP). Diagnosis for each patient was established by the Autism Diagnostic Interview-Revised (ADIR). Postmortem brains from 23 autistic patients (mean interval between death and autopsy: 25.8 hours) and from 16 controls (mean interval between death and autopsy: 20.4 hours) were analyzed. All these brain tissues were scanned by 1.5 Tesla GE MRI system with voxel resolution $1\times1\times1.5$ using a proton density weighted imaging sequence protocol (for more details see [8]).

2.1. Cerebral White Matter Segmentation

Accurate segmentation of cerebral white matter from PD-MRI is a challenge since the gray level distribution of cerebral white matter and surrounding organs is not highly distinguishable. Thus we used a prior learning appearance model of cerebral white matter to control the evolution of the deformable models in the segmentation process.

Conventional deformable model moves in the direction that minimizes the boundary energy E such as e.g. in [9]:

$$E = E_{\text{int}} + E_{\text{ext}} = \int_{k\in\mathbf{K}} \left(\zeta_{\text{int}}\left(\mathbf{b}(\mathbf{P}_k)\right) + \zeta_{\text{ext}}\left(\mathbf{b}(\mathbf{P}_k)\right)\right) dk \quad (1)$$

where $\mathbf{b} = [\mathbf{P}_k : k = 1,\ldots,K]$ be a deformable piecewise-linear boundary with K control points $\mathbf{P}_k = (x_k, y_k, z_k)$, $\zeta_{\text{int}}\left(\mathbf{b}(\mathbf{P}_k)\right)$ and $\zeta_{\text{ext}}\left(\mathbf{b}(\mathbf{P}_k)\right)$ are internal and external forces, respectively.

In this paper we present a new class of the external energy that guided the evolution of deformable model based on learning prior appearance model of cerebral white matter.

Image normalization: To account for monotone (order-preserving) changes of signals (e.g. due to different scanners or sensor characteristics), for each data set, we calculate the occurrence histogram, then we normalize the given data set to make $q_{max} = 255$.

MGRF-based prior appearance model: To exclude any alignment stage before segmentation, the appearance of cerebral white matter is modeled with a translation and rotation invariant generic MGRF with voxel-wise and central-symmetric pairwise voxel interaction specified by a set $\mathbf{N}$ of characteristic central-symmetric voxel neighbor-

hoods $\{\mathbf{n}_\nu : \nu \in \mathbf{N}\}$ on $\mathbf{R}$ and a corresponding set $\mathbf{V}$ of Gibbs potentials, one potential per neighborhood [10].

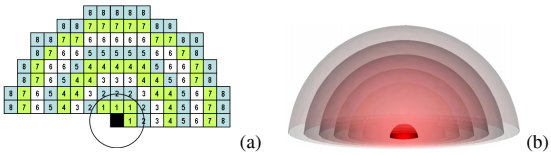

(a) (b)

Fig. 1. Central-symmetric 2D (a) and 3D (b) neighborhoods for the eight distance ranges $[d_{\nu,\min} = \nu - 0.5, d_{\nu,\max} = \nu + 0.5)$; $\nu \in \mathbf{N} = \{1, \ldots, 8\}$ on the lattice $\mathbf{R}$.

A central-symmetric voxel neighborhood $\mathbf{n}_\nu$ embraces all voxel pairs such that (x, y, z)-coordinate offsets between a voxel (x, y, z) and its neighbor (x', y', z') belong to an indexed semi-open interval $[d_{\nu,\min}, d_{\nu,\max})$; $\nu \in \mathbf{N} \subset \{1, 2, 3, \ldots\}$ of the inter-voxel distances: $d_{\nu,\min} \leq \sqrt{(x-x')^2 + (y-y')^2 + (z-z')^2} < d_{\nu,\max}$. Figure 1 illustrates the neighborhoods $\mathbf{n}_\nu$ for the uniform distance ranges $[\nu - 0.5, \nu + 0.5)$; $\nu \in \mathbf{N} = \{1, \ldots, 8\}$.

The interactions in each neighborhood $\mathbf{n}_\nu$ have the same Gibbs potential function $\mathbf{V}_\nu$ of gray level co-occurrences in the neighboring voxel pairs, and the voxel-wise interaction is given with the potential function $\mathbf{V}_{\text{vox}}$ of gray levels in the voxels:

$$\mathbf{V}_{\text{vox}} = [V_{\text{vox}}(q) : q \in \mathbf{Q}]; \{\mathbf{V}_\nu = [V_\nu(q, q') : (q, q') \in \mathbf{Q}^2] : \nu \in \mathbf{N}\} \quad (2)$$

Model identification: Let (x, y, z) denote Cartesian coordinates of points in a finite arithmetic lattice $\mathbf{R} = [(x, y, z) : x = 0, \ldots, X - 1; y = 0, \ldots, Y - 1, z = 1, \ldots, Z - 1]$. It supports a given 3D grayscale image $\mathbf{g} = [g_{x,y,z} : (x, y, z) \in \mathbf{R}; g_{x,y,z} \in \mathbf{Q}]$ with gray levels from a finite set $\mathbf{Q} = \{0, \ldots, Q - 1\}$ and its region map $\mathbf{m} = [m_{x,y,z} : (x, y, z) \in \mathbf{R}; m_{x,y,z} \in \mathbf{L}]$ with region labels from a finite set $\mathbf{L} = \{\mathsf{CWM}, \mathsf{bg}\}$. Each label $m_{x,y,z}$ indicates whether the pixel (x, y, z) in the corresponding data set $\mathbf{g}$ belongs to the goal object (cerebral white matter), $m_{x,y,z} = \mathsf{CWM}$, or to the background, $m_{x,y,z} = \mathsf{bg}$. Let $\mathbf{R}_t = \{(x, y, z) : (x, y, z) \in \mathbf{R} \wedge m_{t;x,y,z} = \mathsf{CWM}\}$ and $\mathbf{C}_{\nu,t}$ denote the part of the 3D lattice $\mathbf{R}$ supporting the training cerebral white matter in the image–map pair $(\mathbf{g}_t, \mathbf{m}_t) \in \mathbf{S}$ and the family of voxel pairs in $\mathbf{R}_t^2$ with the co-ordinate offsets $(\xi, \eta, \gamma) \in \mathbf{n}_\nu$, respectively. Let $\mathbf{F}_{\text{vox},t}$ and $\mathbf{F}_{\nu,t}$ be a joint empirical probability distribution of gray levels and of gray level co-occurrences in the training cerebral white matter from the image $\mathbf{g}_t$, respectively: $\mathbf{F}_{\text{vox},t} = [f_{\text{vox},t}(q) = \frac{|\mathbf{R}_{t,q}|}{|\mathbf{R}_t|}; \sum_{q \in \mathbf{Q}} f_{\text{vox},t}(q) = 1]$ and $\mathbf{F}_{\nu,t} = [f_{\nu,t}(q, q') = \frac{|\mathbf{C}_{\nu,t;q,q'}|}{|\mathbf{C}_{\nu,t}|}; \sum_{(q,q') \in \mathbf{Q}^2} f_{\nu,t}(q, q') = 1]$ where $\mathbf{R}_{t,q} = \{(x, y, z) : (x, y, z) \in \mathbf{R}_t \wedge g_{x,y,z} = q\}$ is a subset of voxels supporting the gray level q in the training cerebral white matter from the image $\mathbf{g}_t$ and $\mathbf{C}_{\nu,t;q,q'}$ is a subfamily of the voxel pairs $\mathbf{c}_{\xi,\eta,\gamma}(x, y, z) = ((x, y, z), (x + \xi, y + \eta, z + \gamma)) \in \mathbf{R}_t^2$ supporting the gray level co-occurrence (q, q') in the same cerebral white matter, respectively.

The MGRF model of the t-th object is specified by the joint Gibbs probability distribution on the sublattice $\mathbf{R}_t$:

$$P_t = \frac{1}{Z_t} \exp(|\mathbf{R}_t|(\mathbf{V}_{\text{vox}}^{\mathsf{T}} \mathbf{F}_{\text{vox},t} + \sum_{\nu \in \mathbf{N}} \rho_{\nu,t} \mathbf{V}_{\nu,t}^{\mathsf{T}} \mathbf{F}_{\nu,t})) \quad (3)$$

where $\rho_{\nu,t} = |\mathbf{C}_{\nu,t}|/|\mathbf{R}_t|$ is the average cardinality of the neighborhood $\mathbf{n}_\nu$ with respect to the sublattice $\mathbf{R}_t$.

To simplify notation, let areas of the training cerebral white matter images be similar, so that $|\mathbf{R}_t| \approx R_{\mathsf{CWM}}$ and $|\mathbf{C}_{\nu,t}| \approx C_{\nu,\mathsf{CWM}}$ for $t = 1, \ldots, T$, where R_{CWM} and $C_{\nu,\mathsf{CWM}}$ are the average cardinalities over the training set $\mathbf{S}$. Assuming the independent samples, the joint probability distribution of gray values for all the training cerebral white matter images is as follows:

$$P_{\mathbf{S}} = \frac{1}{Z} \exp\left(TR_{\mathsf{CWM}}\left(\mathbf{V}_{\text{vox}}^{\mathsf{T}} \mathbf{F}_{\text{vox}} + \sum_{\nu \in \mathbf{N}} \rho_\nu \mathbf{V}_\nu^{\mathsf{T}} \mathbf{F}_\nu\right)\right) \quad (4)$$

where $\rho_\nu = C_{\nu,\mathsf{CWM}}/R_{\mathsf{CWM}}$, and the marginal empirical distributions of gray levels $\mathbf{F}_{\text{vox},\mathsf{CWM}}$ and gray level co-occurrences $\mathbf{F}_{\nu,\mathsf{CWM}}$ describe now all the cerebral white matter images from the training set. Zero empirical probabilities caused by a relatively small volume of the training data available to identify the above model are eliminated if fractions defining the empirical probabilities in terms of cardinalities of the related sublattices or subfamilies are modified as follows: $(\langle\text{nominator}\rangle + \varepsilon)/(\langle\text{denominator}\rangle + S\varepsilon)$. With the Bayesian quadratic loss estimate, $\varepsilon = 1$ and $S = Q$ for the first-order or $S = Q^2$ for the second-order interactions.

Using the analytical approach similar to that in [11], the potentials are approximated with the scaled centered empirical probabilities:

$$\begin{aligned} V_{\text{vox},\mathsf{CWM}}(q) &= \lambda\left(f_{\text{vox},\mathsf{CWM}}(q) - \tfrac{1}{Q}\right); \quad (q) \in \mathbf{Q}; \\ V_{\nu,\mathsf{CWM}}(q, q') &= \lambda\left(f_{\nu,\mathsf{CWM}}(q, q') - \tfrac{1}{Q^2}\right); \quad (q, q') \in \mathbf{Q}^2 \end{aligned} \quad (5)$$

where the common factor λ is also computed analytically. It can be omitted ($\lambda = 1$) if only relative potential values are used for computing relative energies $E_{\nu,\text{rel}}$ of the central-symmetric pairwise voxel interactions in the training data. The energies that are equal to the variances of the co-occurrence distributions:

$$E_{\nu,\text{rel}} = \sum_{q,q' \in \mathbf{Q}^2} f_{\nu,\mathsf{CWM}}(q, q')\left(f_{\nu,\mathsf{CWM}}(q, q') - \frac{1}{Q^2}\right)$$

allow for ranking all the central-symmetric neighborhoods $\mathbf{n}_\nu$ and selecting the top-rank, i.e. most characteristic ones $\mathbf{N}' \subset \mathbf{N}$ to include to the prior appearance model of Eq. (5). Under the model, any grayscale pattern within a deformable boundary $\mathbf{b}$ in an image $\mathbf{g}$ is described by its Gibbs energy

$$E(\mathbf{g}, \mathbf{b}) = \mathbf{V}_{\text{vox},\mathsf{CWM}}^{\mathsf{T}} \mathbf{F}_{\text{vox},\mathsf{CWM}}(\mathbf{g}, \mathbf{b}) + \sum_{\nu \in \mathbf{N}'} \mathbf{V}_{\nu,\mathsf{CWM}}^{\mathsf{T}} \mathbf{F}_{\nu,\mathsf{CWM}}(\mathbf{g}, \mathbf{b}) \quad (6)$$

where $\mathbf{N}'$ is an index subset of the selected top-rank neighborhoods, and the empirical probability distributions are collected within the boundary $\mathbf{b}$ in $\mathbf{g}$.

Boundary evolution using prior appearance model: The following external energy term in Eq. (1) used the learned prior appearance model to guide an evolving boundary in a way such that maximizes the energy within the boundary:

$$\zeta_{ext}\left(\mathbf{b}(\mathbf{P}_k = (x, y, z))\right) = -\pi_{\mathbf{P}}(g_{x,y,z}|\mathbf{S}) \quad (7)$$

where $\pi_{\mathbf{P}}(q|\mathbf{S})$ is the prior conditional probability of the gray level q, given the current gray values in the characteristic central-symmetric neighborhoods of $\mathbf{P}_k$, for the MGRF prior model:

$$\pi_{\mathbf{P}}(g_{x,y,z}|\mathbf{S}) = \frac{\exp\left(E_{\mathbf{P}}(g_{x,y,z}|\mathbf{S})\right)}{\sum_{q \in \mathbf{Q}} \exp\left(E_{\mathbf{P}}(q|\mathbf{S})\right)}$$

where $E_{\mathbf{P}}(q|\mathbf{S})$ is the voxel-wise Gibbs energy for a gray level q assigned to $\mathbf{P}$ and the current fixed gray levels in all neighbors of $\mathbf{P}$ in the characteristic neighborhoods $\mathbf{n}_\nu$; $\nu \in \mathbf{N}$:

$$\begin{aligned} E_{\mathbf{P}}(q|\mathbf{S}) &= V_{\text{vox},\mathsf{CWM}}(q) + \sum_{\nu \in \mathbf{N}} \sum_{(\xi,\eta,\gamma) \in \mathbf{n}_\nu} (V_{\nu,\mathsf{CWM}}(g_{x-\xi,y-\eta,z-\gamma}, q) \\ &+ V_{\nu,\mathsf{CWM}}(q, g_{x+\xi,y+\eta,z+\gamma})) \end{aligned} \quad (8)$$

The evolution of the deformable model terminates after the total energy $E_{\mathbf{r}}$ of the region $\mathbf{r} \subset \mathbf{R}$ inside the boundary $\mathbf{b}$ does not change:

$$E_{\mathbf{r}} = \sum_{\forall \mathbf{P} = (x,y,z) \in \mathbf{r}} E_{\mathbf{P}}(g_{x,y,z}|\mathbf{S}) \quad (9)$$

The deformable boundary $\mathbf{b}$ evolves in discrete time, $\tau = 0, 1, \ldots, T$, as follows:

1. Initialization ($\tau = 0$):
   (a) Initialize a boundary inside the cerebral white matter.
2. Evolution ($\tau \leftarrow \tau + 1$):
   (a) Calculate the total energy of Eq. (9) within the current boundary $\mathbf{b}_\tau$.
   (b) For each control point $\mathbf{P}_k$ on the current boundary, indicate the exterior ($-$) and interior ($+$) nearest neighbors with respect to the boundary [12].
   (c) For each ($+$)-point, calculate the total energy of Eq. (1) for each new candidate for the current control point.
   (d) Select the minimum-energy new candidate.
   (e) Calculate the total energy of Eq. (9) within the boundary that could have appeared if the current control point has been moved to the selected candidate position.
   (f) If the total energy increases, accept this new position of the current control point, otherwise for each ($-$)-point, calculate the total energy of Eq. (1) for each new candidate for the current control point.
   (g) Select the minimum-energy new candidate.
   (h) Calculate the total energy of Eq. (9) within the boundary that could have appeared if the current control point has been moved to the selected candidate position.
   (i) If the total energy increases, accept this new position of the current control point.
   (j) Otherwise do not move the current control point because it is already located on the edge of the cerebral white matter region.
   (k) Mark each voxel visited by the deformable boundary.
   (l) If the current control point moves to the voxel visited earlier, then find the edge formed by the already visited voxels and use the edge points as the new control points of the deformable boundary.
   (m) If the new control points appear, interpolate the whole boundary using cubic splines and then smooth its control points with a low pass filter.
   (n) If the total energy within the boundary does not change, terminate the process; otherwise return to Step 2b.

The proposed segmentation algorithm was tested on a 39 PD-MRI data sets with resolution $512 \times 512 \times 114$. Figure 2 illustrates results of segmenting cerebral white matter shown by axial, sagittal, and coronal cross sections. The pixel-wise Gibbs energies in each cross section are higher for the cerebral white matter than for any other brain tissues. Therefore, our approach separates accurately the cerebral white matter from other background tissues. The evolution terminates after 226 iterations because the changes in the total energy become close to zero. The error of our segmentation with respect to the radiologist "ground truth" is 2.06%. Figure 3 shows more 3D segmentation results of cerebral white matter.

3. SHAPE ANALYSIS OF CEREBRAL WHITE MATTER GYRIFICATIONS AND EXPERIMENTAL RESULTS

We hypothesize that the thickness of gyral cerebral white matter in normal subjects will be greater than in autistic subjects (Fig. 4). To quantify this feature, first we need to extract cerebral white matter gyrifications form the segmented cerebral white matter. In this paper, we developed a new approach to extract cerebral white matter gyrifications automatically from the segmented cerebral white matter. This approach is based on calculating the distance map inside the 3D segmented cerebral white matter using a fast marching level set method [12]. The distance

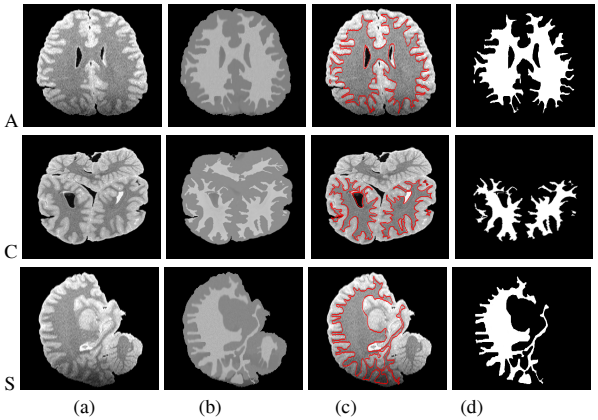

Fig. 2. 3D segmentation of cerebral white matter; results are projected onto 2D axial (A), coronal (C), and saggital (S) planes for visualization: 2D profile of the original PD-MRI images (a), pixel-wise Gibbs energies (b) for $\nu \leq 9$, our segmentation (c), and (d) the radiologist's segmentation.

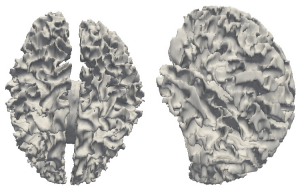

Fig. 3. 3D visualization of the segmented cerebral white matter using the proposed approach

map at any point inside the segmented object is defined as the minimum Euclidian distance from the boundary (Fig. 5). We used our previous LCDG probabilistic model [11] to estimate the marginal density for distances that belong to cerebral white matter gyrifications (class 1) and distances that belong to the other cerebral white matter tissues (class 2) as shown in Fig. 5(b). Using the marginal density, we can extract the cerebral white matter gyrifications by estimating the best threshold that discriminates between the distances from cerebral white matter gyrifications and the distances from the other cerebral white matter tissues as shown in Fig. 6.

For the classification purposes, we use Cumulative Distribution Function (CDF) of the distance map inside the extracted gyrifications of cerebral white matter as a discriminatory shape feature of the CWM structure. Figure 7(a) shows the CDFs for 14 subjects (7 autistics and 7 normals), It is clear from this figure that the two classes, autistic and normal, are completely separable which encouraged us to use the CDFs of distance maps as a discrimination measure between the two classes. In order to use the CDF to classify subjects as control or autistic, the Levy distance was calculated [13]. The Levy distance is defined as the distance between the CDF of the distance map inside the extracted cerebral white matter gyrifications of a given object and the average CDF of the distance map inside the extracted cerebral white matter gyrifications of autistic or normal subjects (Fig. 7(b)). Mathematically, the Levy distance between the CDF of unknown object F_u and the average CDF of autistic/normal subjects $F_{A/N}$ (Fig. 7(c,d)) is defined as follows [13]:

$$\rho(\mathbf{F_u}, \mathbf{F_{A/N}}) = \min_{\alpha>0}\{\alpha : F_{A/N}(d-\alpha) - \alpha \leq F_u(d) \leq F_{A/N}(d+\alpha) + \alpha\} \tag{10}$$

The proposed approach has been applied on 39 data sets (16 normal, and 23 autistic). Accuracy of classification was performed using Chi square test at three confidence levels - 85%, 90% and 95% to examine significant differences in Levy distance. As expected, the 85% con-

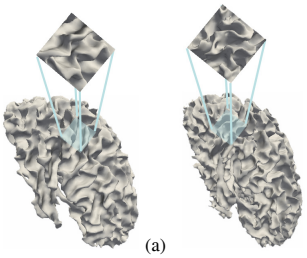

Fig. 4. Segmented cerebral white matter in a control case (a) and in an autistic patient (b). Note that the gyri in the person with autism appear thinner than those of the normal comparison subject.

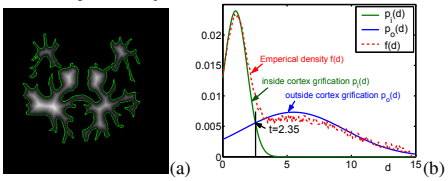

Fig. 5. (a) Coronal section in the 3D distance map for the segmented cerebral white matter (note that the boundary of segmented cerebral white matter shown in green color) and (b) estimated marginal density for each class from the mixed empirical density (normalized histogram) for the distances inside the segmented cerebral white matter.

fidence level yielded the best results - correctly classifying 22/23 autistics, a 0.96 accuracy rate, and 15/16 controls, a 0.94 accuracy rate. At the 90% confidence level, 22/23 autistics were still classified correctly, however, 14/16 controls were correctly classified, bringing the accuracy rate for controls down to 0.88. The 95% confidence level had smaller accuracy rates for both groups; correctly classifying 20/23 autistics, a 0.87 accuracy rate and 14/16 controls, a 0.88 accuracy rate. Overall these results show that the geometric method yields significantly accurate results.

4. CONCLUSION AND FUTURE WORK

In this paper a new geometrical approach for discriminating the autistic and normal control subject has been proposed. It is different from traditional techniques which depend only on volumetric descriptions of different brain structures and are sensitive to the selection of ages and segmentation methods. We will focus on describing the shape of different brain structures such that a discriminating feature can be achieved. Preliminary results for the cerebral white matter comparison have been demonstrated and the Levy distance shows a significant difference between selected normals and autistics. Different brain structures will be investigated in order to follow the development and variations of the autistic brain with time. The investigation will not be limited to the cerebral white matter region but also will include the gray matter study. The approach will be tested on more data sets for more results and validation.

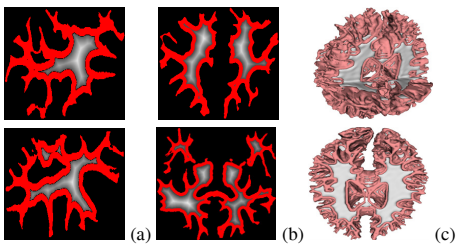

Fig. 6. 2D (a, b) and 3D (c) visualization of the extracted cerebral white matter gyrifications (shown in red (2D) and pink (3D) colors)

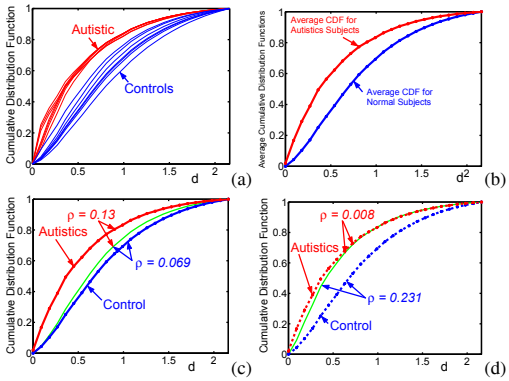

Fig. 7. (a) Cumulative distribution of distance map inside segmented 14 subjects (seven normals and seven autistics), (b) average CDFs for autistic and normal subjects, and (c,d) the proposed classification approach of unknown subjects (green) using Levy distance (ρ); (c) normal, (d) autistic.

5. REFERENCES

[1] J. Lainhart, J. Piven, M. Wzorek, et al., "Macrocephaly in children and adults with autism,"*J Am Acad Child Adolesc Psychiatry*, vol. 36, pp. 282-290, 1997.

[2] M. Yeargin-Allsop, C. Rice, T. Karapurka, N. Doernberg, and C. Boyle,"Murphy C. Prevalence of autism in a US metropolitan area," *JAMA*, vol. 289, pp. 48-55, 2003.

[3] M. Stevens, D. Fein, M. Dunn, et al., "Subgroups of children with autism by cluster analysis: a longitudinal examination," *J Am Acad Child Adolesc Psychiatry*, vol. 39, pp. 346-352, 2000.

[4] T. Kemper and M. Bauman, "The contribution of neuropathologic studies to the understanding of autism," *Neurol Clin*, vol. 11, pp. 175–187, 1993.

[5] B. Egaas, E. Courchesne, and O. Saitoh, "Reduced size of corpus callosum in autism," *Arch Neurol*, vol. 52, pp. 794-801, 1995.

[6] P. Guerin, G. Lyon, C. Barthlmy, et al., "Neuropathological study of a case of autistic syndrome with severe mental retardation," *Dev Med Child Neurol*, vol. 38, pp. 203-211, 1996.

[7] R. Courchesne, R. Carper, and N. Akshoomoff, "Evidence of brain overgrowth in the first year of life in autism," *JAMA*, vol. 290, pp. 337–344, 2003.

[8] C. Schumann, M. Buonocore, and D. Amaral, "Magnetic resonance imaging of the post-mortem autistic brain," *J Autism Dev Disord*, vol. 31, no. 6, pp. 561–568, 2001.

[9] M. Kass, A. Witkin, and D. Terzopoulos, "Snakes: Active contour models," *International Journal of Computer Vision*, vol. 1, pp. 321–331, 1987.

[10] A. El-Baz, A. A. Farag, G. L. Gimel'farb, R. Falk, M. Abou El-Ghar, T. Eldiasty, "A Framework for Automatic Segmentation of Lung Nodules from Low Dose Chest CT Scans," *Proc. of IEEE International Conference on Pattern Recognition (ICPR06)*, Hong Kong, pp. 611–614, 2006.

[11] A. A. Farag, A. El-Baz, and G. Gimelfarb, "Precise Segmentation of Multi-modal Images," *IEEE Transactions on Image Processing*, vol. 15, no. 4, pp. 952–968, 2006.

[12] D. Adalsteinsson and J. Sethian,"A fast level set method for propagating interfaces," *Journal of Computational Physics*, vol. 118, pp. 269–277, 1995.

[13] J. W. Lamperti, *Probability*, J. Wiley & Sons, New York, 1996.